Uncertainty Discourse and Applications

www.uda.reapress.com

Uncert. Disc. Appl. Vol. 3, No. 3 (2026) 188–211.

Paper Type: Original Article

Fractional-Order General Type-2 Fuzzy Control with Adaptive Type-Reduction for Load Frequency Control in Multi-Area Renewable-Based Power Systems with Communication Delays

Abolfazl Fereydoni[1], Seyedeh Fatemeh Faghidian[2,*]

[1] Department of Electrical Engineering and Computer, Arak University of Technology, Arak, Iran; abolfazl.fariduni005@sharif.edu.

[2] Department of Industrial Engineering, Science and Research Branch, Islamic Azad University, Tehran, Iran; f.faghidian@yahoo.com.

Citation:

Received: 17 January 2026 *Revised: 22 April 2026* *Accepted: 10 June 2026*	Fereydoni, A., & Faghidian, S. F. (2026). Fractional-order general Type-2 fuzzy control with adaptive type-reduction for load frequency control in multi-area renewable-based power systems with communication delays. *Uncertainty Discourse and Applications, 3*(3), 188-211.

Abstract

This study investigates a Load Frequency Control (LFC) framework for a three-area renewable-based power system interconnected through tie-lines and subject to communication delays. The proposed framework integrates an open-loop dynamic model, an α-plane-based General Type-2 Fuzzy inference System (GT2FS), three type-reduction approaches (Nie–Tan (NT), Karnik–Mendel (KM), and a causal fractional-order post-filter) and a delay-dependent selection strategy. The framework further incorporates multi-objective parameter optimization and closed-loop performance evaluation. The baseline system comprises three interconnected areas arranged in a ring topology and accounts for Governor Dead Bands (GDBs), soft constraints on the turbine power rate of change, and five distinct communication delay values. The numerical accuracy of the type-reduction methods was assessed against benchmark results. The fractional-order post-filter reproduced the NT output with a reported maximum absolute error of zero, while the iterative KM algorithm achieved an exact match based on direct identification of the switching points. Multi-Objective Particle Swarm Optimization (MOPSO) produced a Pareto archive containing seven solutions, from which a compromise solution was selected, yielding an Integral of Time-weighted Absolute Error (ITAE) of 81.722190, an Integral of Squared Error (ISE) of 0.6906788, and a Total Variation (TV) of 25.089462. However, closed-loop simulations indicate that the performance of the proposed controller, under the current parameter calibration, is not uniformly superior to that of the benchmark configurations. Specifically, the ITAE of the FOGT2-Adp controller exceeded that of the FOGT2-b1 variant in all four evaluated scenarios. Moreover, the frequency-deviation constraint was violated in the Photovoltaic (PV) scenario, and none of the controllers maintained stability at communication delays of 150 and 200 ms. Linearized pole analysis indicated that four controller configurations, excluding the Proportional–Integral–Derivative (PID) controller, satisfied the stability criterion used in the analysis. Nevertheless, this result does not, by itself, establish the stability of the nonlinear closed-loop system under communication delays and actuator saturation. Overall, the findings support the numerical consistency of the evaluated type-reduction implementations and demonstrate the functional role of fractional-order memory within the proposed framework. However, they do not establish the universal superiority of the adaptive controller or its robustness to substantial communication delays.

Keywords: Load frequency control, General Type-2 fuzzy sets, Adaptive type-reduction, Fractional-order control, Communication delays, Renewable-based power systems.

1 | Introduction

Load Frequency Control (LFC) plays a critical role in maintaining the balance between power generation and load demand while ensuring that power exchanges through tie-lines remain within their scheduled limits. The

Corresponding Author: f.faghidian@yahoo.com

https://doi.org/10.48313/uda.v3i3.107

Licensee System Analytics. This article is an open access article distributed under the terms and conditions of the Creative Commons Attribution (CC BY) license (http://creativecommons.org/licenses/by/4.0).

increasing penetration of wind and Photovoltaic (PV) generation, the associated reduction in effective system inertia, and the growing reliance on communication networks for measurement and control signal transmission have made frequency regulation increasingly sensitive to generation uncertainty and communication delays. Previous studies have investigated a range of control strategies to address these challenges, including interval Type-2 fuzzy controllers, fractional-order controllers, and metaheuristic optimization techniques for controller parameter tuning. Representative examples include fractional-order fuzzy controllers for islanded microgrids [1], fractional-order Type-2 structures for hybrid systems [2], combinations of parallel control architectures and fractional-order fuzzy logic for Automatic Generation Control (AGC) [3], and adaptive fractional-order strategies for renewable-integrated power networks [4].

In parallel, general Type-2 fuzzy controllers have been investigated as a means of representing uncertainty in membership functions more comprehensively [5]. Fractional-order Type-2 approaches incorporating Particle Swarm Optimization (PSO) have also been evaluated in systems subject to time delays [6]. More recent studies have explored adaptive Type-2 control strategies for frequency regulation under the uncertainty associated with renewable energy sources [7], as well as multi-loop Type-2 control architectures incorporating fractional-order components for interconnected microgrids [8]. Nevertheless, the numerical performance reported in individual studies depends on the underlying system model, system scale, disturbance profiles, simulation horizon, performance indices, and controller calibration. Consequently, quantitative results obtained from different systems cannot be meaningfully ranked or compared without a common benchmark and consistent evaluation conditions.

Against this background, the present study develops an integrated framework comprising three principal components: 1) A General Type-2 Fuzzy inference System (GT2FS) employing five linguistic labels and an α-plane representation, 2) Three type-reduction approaches—Nie–Tan (NT), Karnik–Mendel (KM), and a fractional-order post-filter—combined with a delay-dependent selection strategy, and 3) The multi-objective tuning and closed-loop evaluation of a fractional-order fuzzy controller. The framework is designed to examine the numerical consistency of the implemented type-reduction methods and assess controller performance under different operating scenarios and communication delays. Particular emphasis is placed on distinguishing numerical validation from closed-loop performance and stability assessment. Accordingly, conclusions regarding controller superiority and stability are restricted to the evidence obtained under the specified modelling assumptions, parameter settings, and simulation conditions.

2 | Power System Model and Open-Loop Validation

2.1 | Topology and Parameters

The base system consists of three areas connected in a ring configuration: Area 1 ↔ Area 2 ↔ Area 3 ↔ Area 1. Each area is represented by an aggregated model comprising a governor, a turbine, and the swing equation. Area 1 includes a thermal power plant and wind generation, along with an aggregation of electric vehicles; Area 2 consists of a hydropower plant, a PV system, and a battery energy storage system; and Area 3 comprises a gas power plant, a fuel cell, an alkaline electrolyser, and a flywheel. The synchronizing coefficients for the tie-lines are set as follows: $T_{12} = 0.20$, $T_{23} = 0.15$, and $T_{31} = 0.18$.

Table 1. Basic parameters of the three-area system.

Parameters	Area 1	Area 2	Area 3
Inertia H(s)	0.1667	0.1000	0.1200
Damping D (p.u./Hz)	0.0150	0.0200	0.0180
Governor Time Constant Tg (s)	0.08	0.20	0.15
Turbine time constant Tt (s)	0.30	0.50	0.35
Droop R (Hz/p.u.)	2.40	2.50	2.30
Bias B (p.u./Hz)	0.425	0.450	0.430
GRC (p. u./s)	0.10	0.05	0.10

The Generation Dead Band (GDB) is 0.05 Hz, and the governor command limit is ±0.30 p.u. The model employs a soft limiter for the turbine power rate of change based on the TANH function; therefore, this numerical approximation should be distinguished from a hard limiter. All states are initialized to zero at $t = 0$. An open-loop simulation was conducted for 60 seconds on the 6001-bus network, with an output step size of 0.01 seconds. The ode45 solver was used for the delay-free case, while a delay-aware solver was employed for the case involving delays; a standalone Simulink implementation—utilizing ode45 and delay blocks—was also evaluated.

2.2 | Dynamic Equations

The state vector for each area includes frequency deviation, turbine mechanical power, and the governor command:

$$x_i = \left[\Delta f_i,\ \Delta P_{m,i},\ \Delta P_{gov,i}\right]^{\top}, \quad i \in \{1,2,3\}. \tag{1}$$

The swing equation incorporates renewable power generation, load, interconnector exchange, and damping:

$$2H_i \frac{d\Delta f_i}{dt} = \Delta P_{m,i} + \Delta P_{RES,i} - \Delta P_{L,i} - \Delta P_{tie,i} - D_i \Delta f_i. \tag{2}$$

The effective error input to the governor is accurately modeled using GDB:

$$\Delta f_{GDB,i}(\Delta f_i) = \begin{cases} 0, & |\Delta f_i| \le \text{GDB}, \\ \Delta f_i - \text{GDB}\,\text{sign}(\Delta f_i), & |\Delta f_i| > \text{GDB}. \end{cases} \tag{3}$$

$$\frac{d\Delta P_{gov,i}}{dt} = \frac{-\Delta f_{GDB,i}/R_i - \Delta P_{gov,i}}{T_{g,i}}. \tag{4}$$

The turbine input rate is limited via soft saturation to ensure that the Generation Rate Constraint (GRC) limit is met in the first instance:

$$u_{GRC,i} = GRC_i \tanh\left(\frac{\Delta P_{gov,i} - \Delta P_{m,i}}{T_{t,i}\, GRC_i}\right), \quad \frac{d\Delta P_{m,i}}{dt} = u_{GRC,i}. \tag{5}$$

Along the link ij, a delay is applied to the received frequency. In the baseline case, $\tau_{ij} = 0$, while in delay scanning, a common value τ is considered:

$$\frac{d\Delta P_{tie,ij}}{dt} = 2\pi T_{ij}\left[\Delta f_i(t) - \Delta f_j\left(t - \tau_{ij}\right)\right], \quad ij \in \{12,23,31\}. \tag{6}$$

The model incorporates three nonlinearities: An explicitly modeled governor deadband, a soft GRC limiter, and a governor command limit. The governor command limit was not activated under the disturbances applied to the baseline model. This finding is specific to the small-magnitude disturbances considered in the present analysis and should not be extrapolated to scenarios involving larger or more severe disturbances.

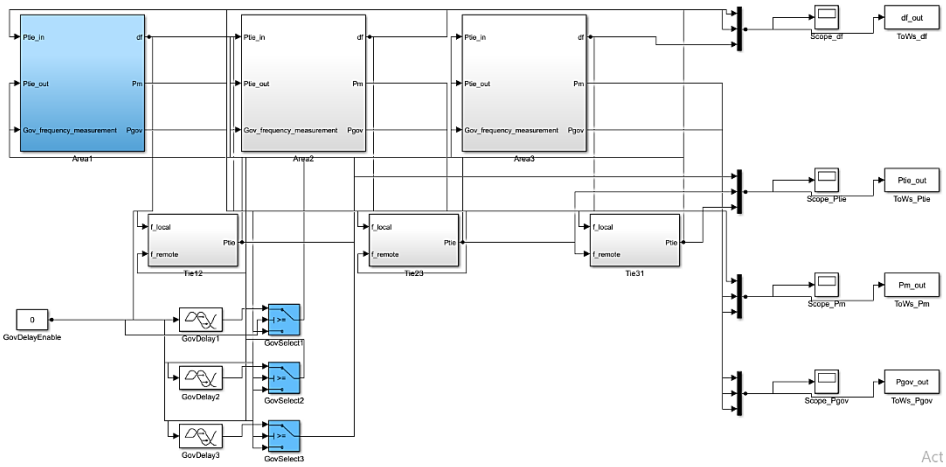

Fig. 1. Engineering model of a three-area power system with a ring structure.

As shown in *Fig. 1*, Area 1 includes a thermal power plant, wind power, and an aggregation of electric vehicles. Area 2 includes a hydroelectric power plant, PVs, and battery storage. Area 3 includes a gas-fired power plant, a fuel cell, an alkaline electrolyser, and a flywheel. The tie-line coefficients are $T_{12} = 0.20$, $T_{23} = 0.15$, and $T_{31} = 0.18$.

2.3 | Open-Loop Scenarios

Table 2. Base model deterministic scenarios.

Scenarios	Disturbance	Place and Time
S1	Load step +0.1 p.u.	Area 1, t=10s
S2	$0.05\sin(0.2\pi t) + 0.02\sin(\pi t) \pm 0.10$ p.u.	Wind in Area 1, from t=10s
S3	PVC step with a value of +0.08 p.u.	Area 2, t=30s
S4	Combination of S1, S2, and S3	All of the above

2.4 | Open-Loop Results and Physical Analysis

In the step-load scenario, the maximum absolute frequency deviations in Areas 1, 2, and 3 were 0.1815888696 Hz, 0.1607677882 Hz, and 0.1687669125 Hz, respectively, while the maximum tie-line power deviation was 0.05400969053p.u. At [time to be specified], the frequency deviations in Areas 1, 2, and 3 were −0.1275122359 Hz, −0.1108743745 Hz, and −0.1313356948 Hz, respectively. The final discrepancy was 0.0204613204 Hz. Because secondary Automatic Generation Control (AGC) is inactive in the baseline model, the system state at [time to be specified] cannot be regarded as a verified steady state.

In the wind scenario, the maximum frequency deviations in the three areas were 0.1207079814Hz, 0.1309725371Hz, and 0.1358342313Hz, and the maximum tie-line power was reported as 0.03898786106p.u. The final values were -0.03388383831Hz, -0.07926832381Hz, and -0.08834699974Hz, respectively, with a final discrepancy of 0.0544631614Hz. The oscillatory and bounded nature of the wind disturbance results in a response that is smoother yet more oscillatory. In the PV step scenario, the maximum absolute frequency deviations in areas 1 through 3 were 0.1397334902, 0.1905673228, and 0.1473227631 Hz, respectively, while the maximum tie-line power was 0.06379595528p.u. The final values were +0.1185087119, +0.06499525771, and +0.1313140045Hz, with a final deviation of 0.0663187468 Hz. The positive sign is consistent with the interpretation that an increase in PV generation acts as a net reduction in load.

In the combined scenario, the maximum frequency deviations were 0.1852248572, 0.2038793548, and 0.2167180939Hz, and the maximum tie-line power was 0.1063107815p.u. The final values were -0.06310970256, -0.06719563367, and -0.1036986276 Hz, with a final deviation of 0.040588925 Hz.

Consequently, the combined scenario produced the highest single-area peak for the base model as well as the greatest stress on the tie-line.

In the single-area model with a load of 0.1 p.u., the analytical value for the steady-state frequency—accounting for the Governor Dead Band (GDB)—was -0.279922779923 Hz. ode45 yielded a value of -0.279922779984 Hz, with an absolute error of $6.13663009297\times10^{-11}$ Hz—a value significantly smaller than the 10^{-3}Hz limit. In the three-area model, the analytical equilibrium was -0.124629196 Hz, while the numerical average at t=60 s was -0.123240768 Hz; the difference is 0.00138842712 Hz, which exceeds the 10^{-3} Hz agreement threshold. This discrepancy must be explicitly acknowledged and should not be presented as a perfect match.

In the single-area model with a 0.1 p.u. load, the analytical steady-state frequency—accounting for GDB—was -0.279922779923 Hz; `ode45` yielded a value of -0.279922779984 Hz, with an absolute error of $6.13663009297\times10^{-11}$ Hz—a value significantly smaller than the 10^{-3} Hz limit. In the three-area model, the analytical equilibrium was -0.124629196 Hz, while the numerical average at t=60s was -0.123240768 Hz; the difference is 0.00138842712 Hz, which exceeds the 10^{-3} Hz agreement threshold. This discrepancy must be explicitly acknowledged and should not be presented as a perfect match.

In an independent comparison of Simulink, the maximum absolute difference relative to MATLAB was reported as $2.4 * 10^{-7}$ for the load-step scenario and $9.2 * 10^{-5}$ for the delay sweep. These findings support the numerical consistency between the two implementations within the specified tolerances; however, the discrepancy regarding the terminal frequency criterion in the three-area model persists.

2.5 | The Effect of Communication Delay in the Base Model

For Scenario 1, a delay of $\tau \in 0.50, 100, 150, 200$ ms was applied. The maximum Δf_1 increased as the delay increased, rising from 0.18158887 to 0.20567723, 0.50758020, 0.89603921, and 1.10980591 Hz; the maximum values across all areas were 0.18158887, 0.35942208, 0.67855475, 1.32501995, and 1.62017753 Hz, respectively. At larger delays, a sign change in the final frequency value indicates oscillatory behaviour induced by the delay. These results demonstrate the necessity of explicitly accounting for delay when evaluating the controller.

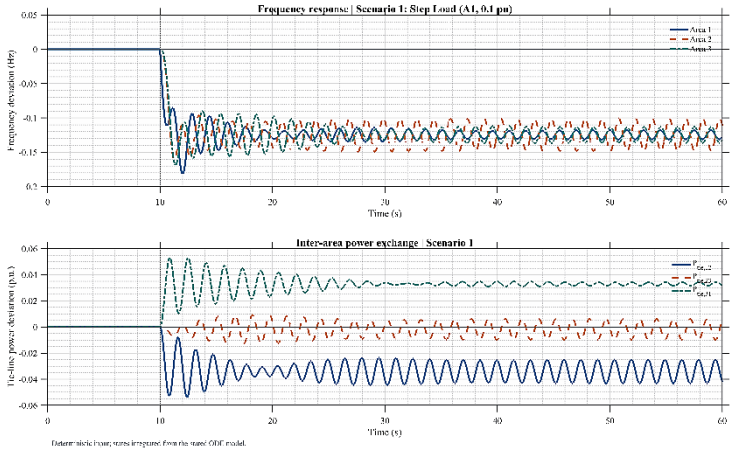

Fig. 2. Response of Scenario 1 to a 0.1 p.u. step load in Area 1 at t=10s; top: Frequency deviation of the areas, and bottom: Tie-line power deviation.

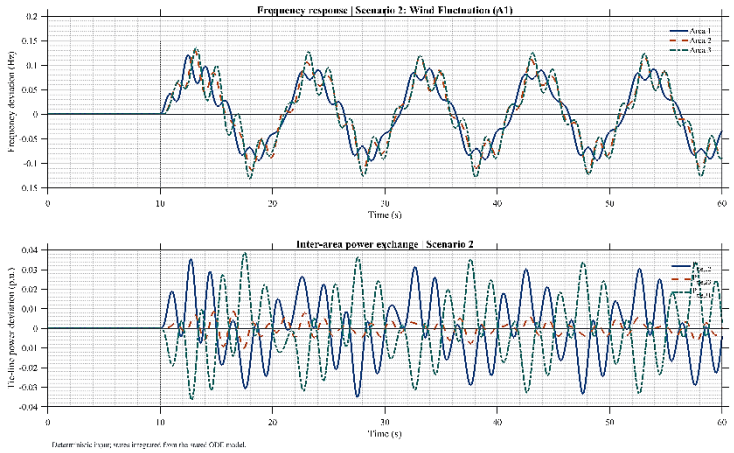

Fig. 3. Response of Scenario 2 to a constrained wind power fluctuation in Area 1 starting at t=10s; top: Area frequency deviations, and bottom: Tie-line power deviations.

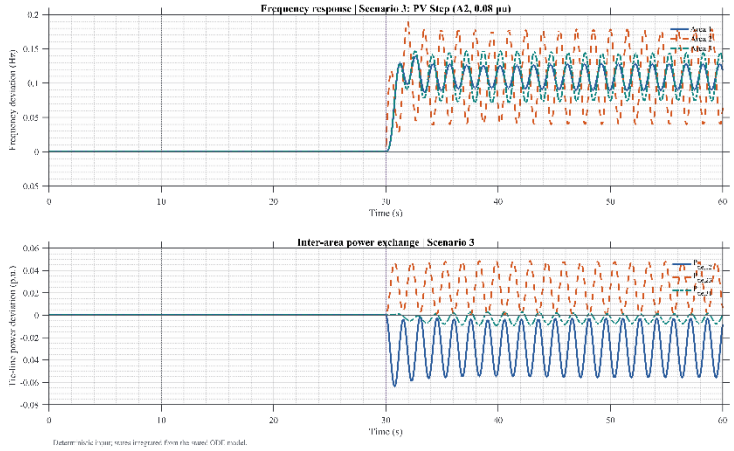

Fig. 4. Response of Scenario 3 to a 0.08 p.u. step change in PV generation in Area 2 at t=30s; top: Frequency deviation, and bottom: Tie-line power deviation.

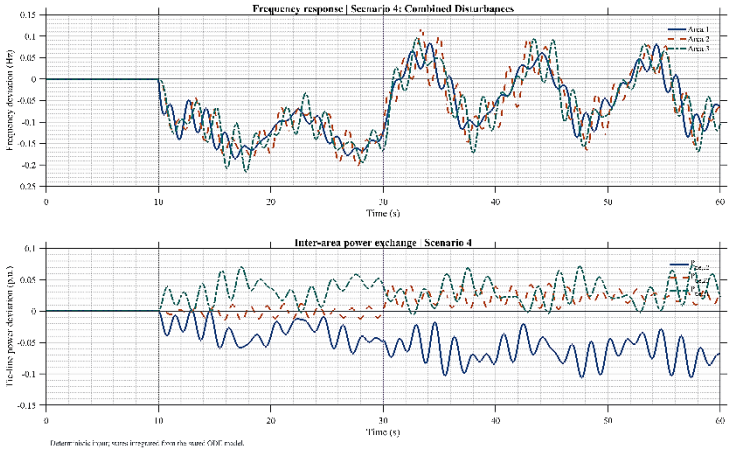

Fig. 5. Response of Scenario 4 to the combined disturbances of Scenarios 1, 2, and 3; top: Area frequency deviations, and bottom: Tie-line power deviations.

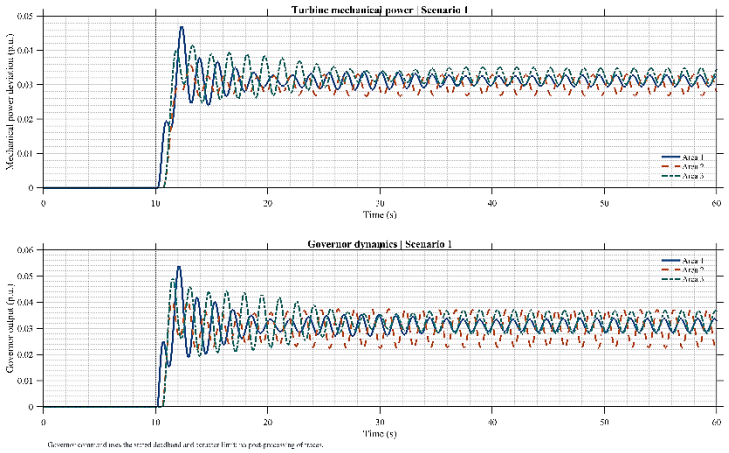

Fig. 6. Turbine mechanical power and governor power command in Scenario 1.

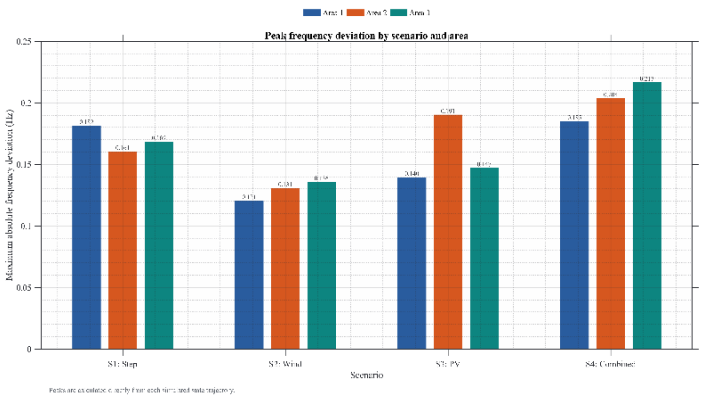

Fig. 7. Bar chart of the maximum absolute value of frequency deviation for the four base-model scenarios.

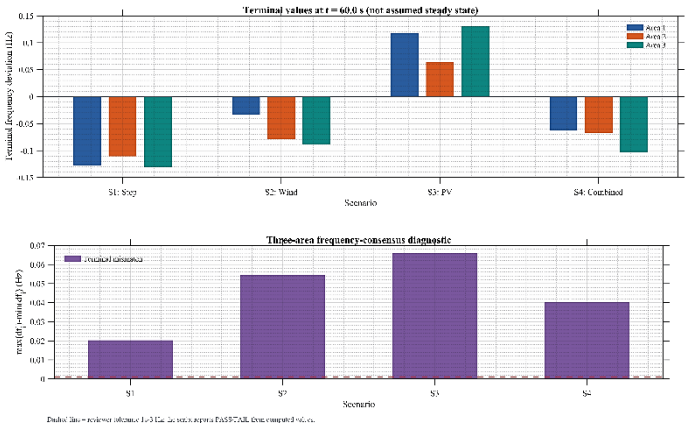

Fig. 8. Bar chart of terminal frequency at t=60s for the four base-model scenarios.

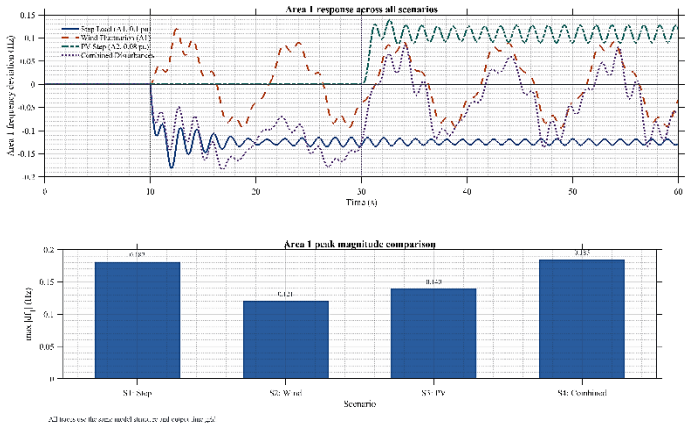

Fig. 9. Comparison of frequency deviation in Area 1 across four scenarios on a common axis.

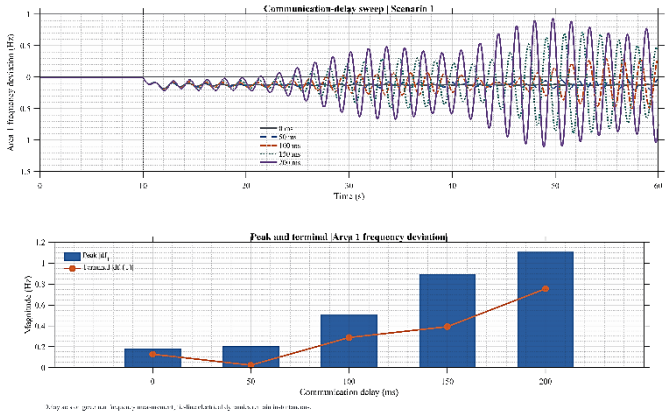

Fig. 10. Effect of communication delay τ = 0, 50, 100, 150, and 200 ms on the frequency response of Area 1 in Scenario 1.

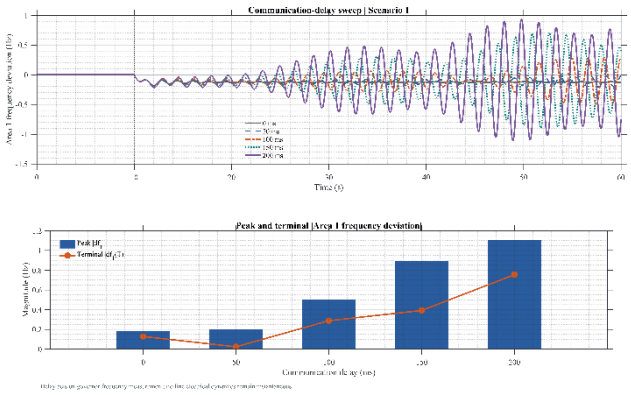

Fig. 11. Validation of the single-area steady-state condition, accounting for the generation deadband: Analytical value -0.279922779923 Hz, numerical value -0.279922779984 Hz, and an absolute error of $6.13663009297 \times 10^{-11}$ Hz, which is below the 10^{-3} Hz threshold.

3 | General Type-2 Fuzzy Structure and Adaptive Type-Reduction

3.1 | Membership Functions and α-Planes

The fuzzy input vector consists of the control error E and the change in error CE. Five linguistic labels—NB, NS, Z, PS, and PB—are defined, with centers at -1.00, -0.50, 0.00, 0.50, and 1.00; a width of w = 0.30;

and a mean uncertainty half-width of $\Delta m = 0.10$. Four α levels are set at 0.25, 0.50, 0.75, and 1.00, and the MacVicar–Whelan rule base comprises 25 rules. The maximum value of the UMF is reported as 1.000, while the maximum value of the LMF is 0.667.

$$t_1(x) = \max\left(1 - \frac{|x - (c - \Delta m)|}{w}, 0\right), \quad t_2(x) = \max\left(1 - \frac{|x - (c + \Delta m)|}{w}, 0\right). \tag{7}$$

$$\mathrm{UMF}(x) = \max(t_1, t_2), \quad \mathrm{LMF}(x) = \min(t_1, t_2), \quad H(x) = \frac{1}{2}[\mathrm{UMF}(x) + \mathrm{LMF}(x)]. \tag{8}$$

$$lo_\alpha(x) = (1 - \alpha)\mathrm{LMF}(x) + \alpha H(x), \quad up_\alpha(x) = (1 - \alpha)\mathrm{UMF}(x) + \alpha H(x). \tag{9}$$

$$y = \frac{\sum_a \alpha_a y_{\alpha_a}}{\sum_a \alpha_a}. \tag{10}$$

In each α-plane, the lower and upper membership degrees are calculated as a combination of the LMF/UMF and an intermediate function H; the final output is obtained via a weighted average based on the α-level. Due to uncertainty in the mean, the UMF of each label may exhibit two symmetric peaks flanking the nominal centre; this characteristic is preserved within the membership function data.

3.2 | Rule Base and Activation Power

$$\mathrm{rule}_{\mathrm{map}} = \begin{bmatrix} 1 & 1 & 1 & 2 & 3 \\ 1 & 1 & 2 & 3 & 4 \\ 1 & 2 & 3 & 4 & 5 \\ 2 & 3 & 4 & 5 & 5 \\ 3 & 4 & 5 & 5 & 5 \end{bmatrix}. \tag{11}$$

$$y_{\mathrm{conseq}} = \{-1.0, -0.5, 0.0, +0.5, +1.0\}, \quad f_{r,l} = \min\big(lo_\alpha(E), lo_\alpha(CE)\big), \quad f_{r,u} = \min\big(up_\alpha(E), up_\alpha(CE)\big). \tag{12}$$

At the point E=0.30, CE=0.10, and α=0, only two rules—with the values shown in the figure—are activated: Rule 13, with a lower strength of 0.3333 and an upper strength of 0.6667; and Rule 18, with a lower strength of 0 and an upper strength of 0.6667. In the reference test case where α=0.5, the strengths are as follows: f_{13},l=1/12, f_{13},u=1/4, f_{18},l=1/6, and f_{18},u=1/2.

3.3 | Type Reduction Methods

In the NT method, the output for each α-level is the weighted average of the rule consequences, using the sum of the lower and upper strengths. If the denominator is less than 10^{-12}, an output of zero is returned.

$$y_\alpha^{\mathrm{NT}} = \frac{\sum_{r=1}^{25}\big(f_{r,l} + f_{r,u}\big)\, y_{\mathrm{conseq},r}}{\sum_{r=1}^{25}\big(f_{r,l} + f_{r,u}\big)}. \tag{13}$$

In the KM method, the lower and upper bounds are calculated by iterating over the switching point k within the sorted consequences. Subsequently, the midpoint $\frac{y_l + y_u}{2}$ is taken as the output for a given α-level, and the α-weighted average is used as the final output.

$$y_l = \frac{\sum_{r \le k} f_{r,u}\, y_r + \sum_{r > k} f_{r,l}\, y_r}{\sum_{r \le k} f_{r,u} + \sum_{r > k} f_{r,l}}. \tag{14}$$

$$y_u = \frac{\sum_{r \le k} f_{r,l}\, y_r + \sum_{r > k} f_{r,u}\, y_r}{\sum_{r \le k} f_{r,l} + \sum_{r > k} f_{r,u}}. \tag{15}$$

The fractional block FR is applied to the output time series NT. The weight of each sample is defined by the time interval and the fractional order β, while an exponential factor with a constant $T_f = 0.1s$ limits the memory:

$$w_j = (t_k - t_j)^{\beta-1}\exp\left[-\frac{t_k - t_j}{T_f}\right], \quad y_{mem}(t_k) = \frac{\sum_{j<k} w_j\, y_{NT}(t_j)}{\sum_{j<k} w_j}. \tag{16}$$

$$y_{FR}(t_k) = (1-\beta)y_{mem}(t_k) + \beta y_{NT}(t_k). \tag{17}$$

At β=1, the FR block reduces exactly to NT; as β approaches zero, the contribution of the causal memory increases. The selection policy is as follows: The NT method for $\tau_d < 0.05$s; the FR method with β=0.5 for $0.05 \le \tau_d < 0.15$s; and the KM method for $\tau_d \ge 0.15$s. While this rule dictates the algorithm selection, it does not, by itself, guarantee closed-loop stability or robustness against large delays.

$$\text{select}(\tau_d) = \begin{cases} \text{NT}, & \tau_d < 0.05\,\text{s}, \\ \text{FR } (\beta = 0.5), & 0.05 \le \tau_d < 0.15\,\text{s}, \\ \text{KM}, & \tau_d \ge 0.15\,\text{s}. \end{cases} \tag{18}$$

3.4 | Numerical Validation of Blocks

Three independent tests were conducted to verify the implementation of the control method. First, the maximum absolute error between the FR method (with $\beta = 1$) and the NT output was found to be $0.000000*10^0$. Second, at the point $E, CE, \alpha = 0.30, 0.10, 0.50$, both the direct counting of switching points and the iterative KM algorithm yielded $y_l = 0.20000000$ and $y_u = 0.42857143 = 3/7$; the difference between the two bounds was zero. Third, due to the symmetry of the rule base, the outputs of both the NT and KM methods at the origin $E, CE = 0,0$ were +0.00000000.

In a static sweep with $CE = 0$ and 201 points ranging from -1 to +1, the mean value of y_{NT-E} was 0.0527, while the mean value of y_{KM-E} was 0.0497. The maximum difference between the NT and KM outputs was 0.0097, and the output bounds for both methods were 1.0000pm. A dynamic test was performed using $E(t) = 0.8\sin 2\pi \cdot 0.3t$ and $CE(t) = [Et(k) - Et(k-1)]/\Delta t$, with $\Delta t = 0.05s$ over the interval [0, 10]s. The Root Mean Square Error (RMSE) was 0.0045 between the NT and KM methods, 0.2527 between the NT and FR methods (with β =0.5), and 0.3438 between the NT and FR methods (with $\beta = 0.2$). This discrepancy reflects the effect of fractional memory, rather than necessarily an improvement in the final control criterion. The reported computational time for each evaluation is 14.987792 ms for NT and 15.247681 ms for KM, representing a 1.02 ratio. These figures are specific to the implementation and hardware tested; they should not be generalized to other systems without information regarding an identical computing environment.

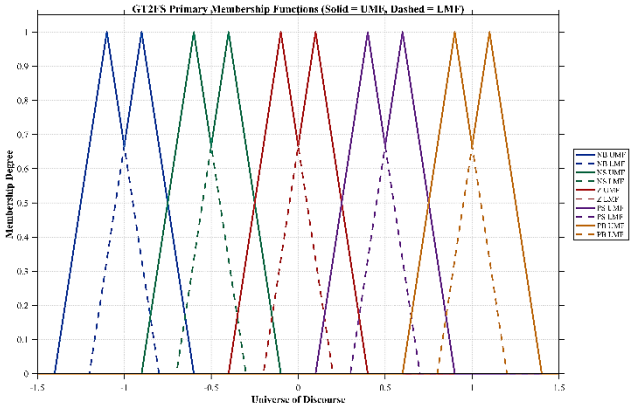

Fig. 12. Initial membership functions of a general type-2 fuzzy set; the solid curves represent the UMF, and the dashed curves represent the LMF.

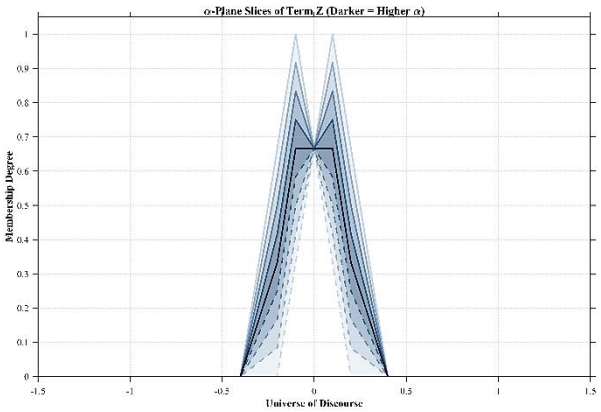

Fig. 13. α-planes for the label Z; the membership level varies from α=0 to α=1, reaching the intermediate function H at α=1.

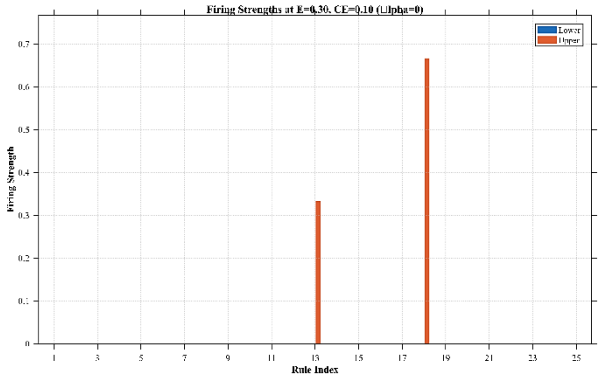

Fig. 14. Low and high activation strengths for 25 rules at E=0.30, CE=0.10, and α=0; only two rules have non-zero activation strengths.

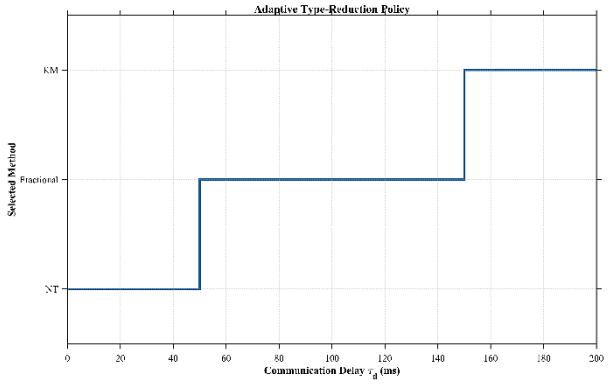

Fig. 15. Adaptive selection policy of the type reduction method in terms of communication delay τd.

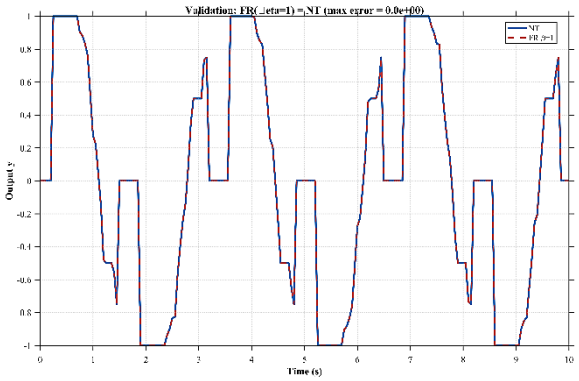

Fig. 16. Validation of the fractional block at β=1 against the NT output; the maximum recorded absolute error is 0.

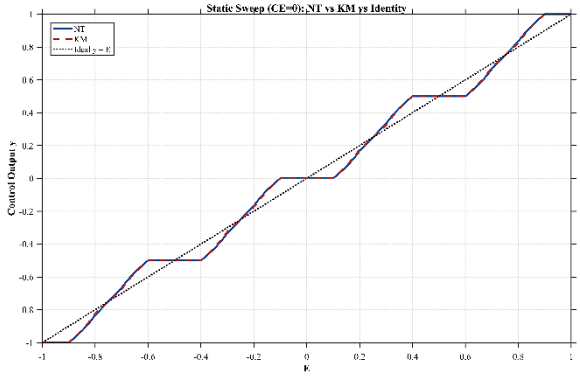

Fig. 17. Static scan with CE=0: NT and KM outputs compared to the reference line y=E.

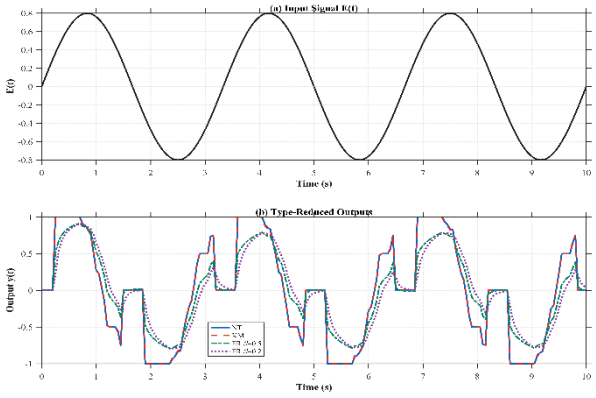

Fig. 18. Dynamic test: Input signal E(t) and the outputs of NT, KM, and the fractional filter FR for β=0.5 and β=0.2.

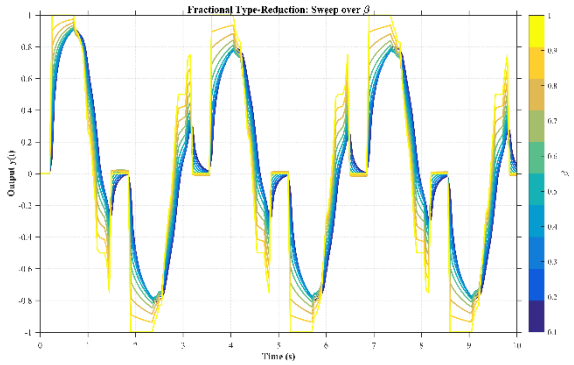

Fig 19. Sweeping the fractional parameter β for values from 0.1 to 1.0; at β=1, the output coincides with the NT result.

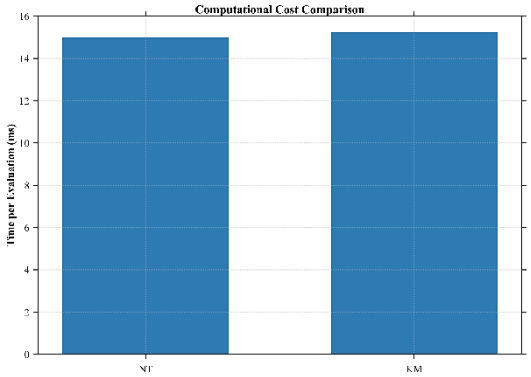

Fig. 20. Comparison of the computational time per evaluation for NT and KM; the values are 14.987792 ms and 15.247681 ms, respectively.

4 | Optimization Formulation and Parameter Tuning

The parameters of the fuzzy fractional-order controller—eight in total—are represented by a vector Θ. Multi-objective optimization was performed using Multi-Objective Particle Swarm Optimization (MOPSO) to generate a Pareto archive, while Genetic Algorithm (GA) and PSO were evaluated as methods based on a weighted-cost function. In the reported experiment, MOPSO was executed with a population size of 15, 25 iterations, and 375 evaluations; the GA was run with a population of 15 and 25 iterations (incorporating elitism), and the PSO was executed with a population of 15 and 25 iterations. To assess repeatability, 10 independent PSO runs were conducted, each with a population size of 10 and 25 iterations. The simulation parameters are as follows: a time step Δt=0.050s, a time horizon T=20.0s, and a memory length GL of 50.

4.1 | Performance Criteria and Constraint Penalties

The three raw Pareto archive objectives are Integral of Time-weighted Absolute Error (ITAE), Integral of Squared Error (ISE), and Total Variation (TV). ITSE is also used for the purpose of a comparative report:

$$\mathrm{ITAE} = \Delta t \sum_{k} t_k \left[\sum_{i=1}^{3} |\Delta f_i(k)| + \sum_{i=1}^{3} \left|\Delta P_{tie,i}(k)\right| \right]. \tag{19}$$

$$\mathrm{ISE} = \Delta t \sum_{k} \left[\sum_{i=1}^{3} \Delta f_i(k)^2 + \sum_{i=1}^{3} \Delta P_{tie,i}(k)^2 \right]. \tag{20}$$

$$\mathrm{ITSE} = \Delta t \sum_{k} t_k \sum_{i=1}^{3} \Delta f_i(k)^2, \quad \mathrm{TV} = \sum_{i=1}^{3} \sum_{k} |u_i(k+1) - u_i(k)|. \tag{21}$$

The strict constraints relate to the frequency deviation $|\Delta_f| \leq 0.20$ Hz and the tie-line power deviation $|\Delta P_{tie}| \leq 0.10$ p.u. An incremental penalty with a coefficient of 105 was applied:

$$P_{pen} = 10^5[\max(0, \max|\Delta f| - 0.20) + \max(0, \max|\Delta P_{tie}| - 0.10)]. \tag{22}$$

$$F = \left[\mathrm{ITAE} + P_{pen},\ \mathrm{ISE} + P_{pen},\ \mathrm{TV} + P_{pen}\right]. \tag{23}$$

In GA and PSO, the weighted cost is formulated based on three raw objectives plus the aforementioned penalty term. The uncontrolled baseline case was infeasible due to severe constraint violations; it recorded a cost of 895,105.929999, a maximum Δ_f of 6.505847 Hz, and a maximum ΔP_{tie} of 2.741728 p.u.

4.2 | Optimization Results

The MOPSO archive contained 7 solutions. The ranges were reported as follows: ITAE [80.2939, 83.8939], ISE [0.65561, 0.75757], and TV [23.7056, 26.5612]. A compromise solution—the 5th out of the 7—was selected, having a normalized L2-distance of 0.7145 from the ideal point. Its parameter vector is: Θ^*=0.000000, 1.871288, 2.000000, 0.000000, 1.213327, 1.000000, 0.679925, 0.571083.

The corresponding values were: ITAE = 81.722190, ISE = 0.6906788, TV = 25.089462, maximum $|\Delta f|$ = 0.169317 Hz, maximum $|\Delta P_{tie}|$ = 0.053679 p.u., and the feasibility flag was 1.

In the weighted-cost comparison, GA yielded ITAE = 41.286386, ISE = 0.2785581, ITSE = 2.494403, and TV = 45.969514; the maximum values were $|\Delta f|$ = 0.197900 Hz and $|\Delta P_{tie}|$ = 0.075064 p.u. PSO yielded ITAE = 34.085742, ISE = 0.1708558, ITSE = 1.655889, and TV = 42.675775; the maximum values were Δf = 0.145928 Hz and $|\Delta P_{tie}|$ = 0.062967 p.u. Both solutions were feasible within the reported constraints. These values alone do not establish a definitive, unified ranking among MOPSO, GA, and PSO, as MOPSO optimized a multi-objective vector, whereas GA and PSO optimized a weighted-cost function; this fundamental difference in the objective function must be taken into account when interpreting the comparison.

Over 25 iterations, the best ITAE reported for MOPSO decreased from 265.967268 to 80.293942; the final archive size was 7, representing a relative reduction of 69.81%. The cost for GA decreased from 27.615303 to 25.819880 (6.5%), while the cost for PSO decreased from 29.692369 to 22.237794 (25.1%). In 10 independent runs of PSO, the following statistics were recorded: a mean of 31.1937, a standard deviation of 6.3186, a minimum of 22.9568, a maximum of 37.9097, and a coefficient of variation of 20.26%. Consequently, the results exhibit significant dispersion, and the outcome of a single run should not be presented as the definitive result for all runs.

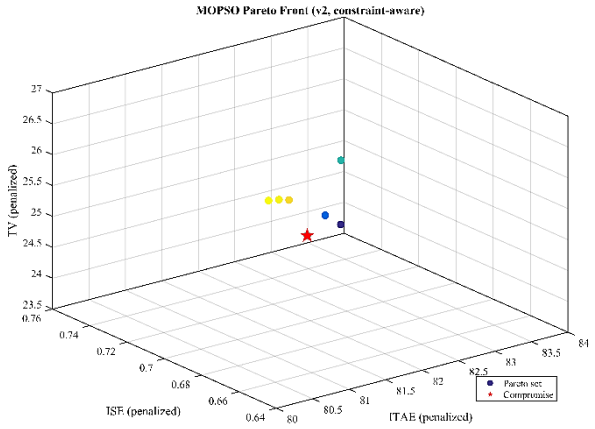

Fig. 21. 3D Pareto front of MOPSO with penalized objectives; the archive contains 7 solutions.

According to *Fig. 21*, the range for ITAE is [80.2939, 83.8939], for ISE is [0.65561, 0.75757], and for TV is [23.7056, 26.5612]; a compromise solution is indicated.

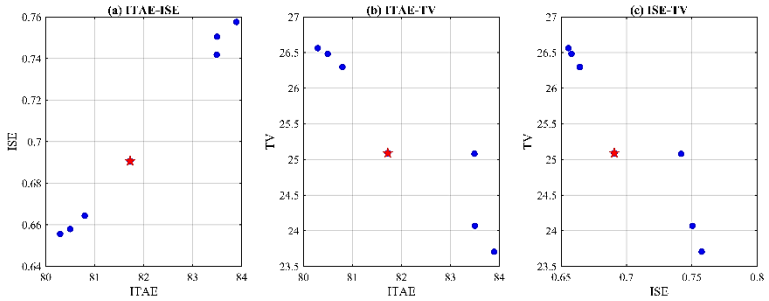

Fig. 22. Two-dimensional plots of the Pareto archive.

According to *Fig. 22*, the correlation between ITAE and ISE is reported as 0.997, the correlation between ITAE and TV as -0.938, and the correlation between ISE and TV as -0.944.

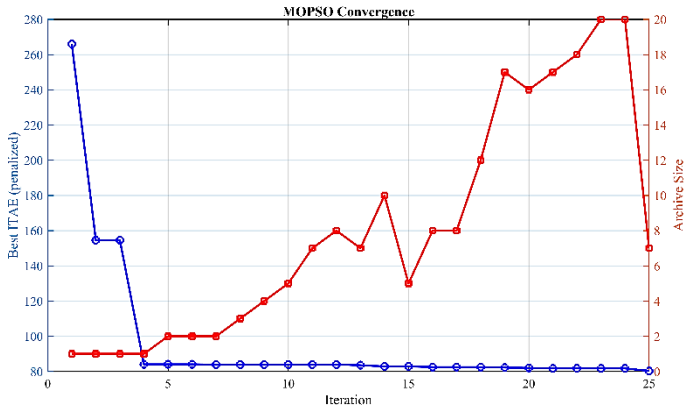

Fig. 23. MOPSO convergence history; the best ITAE improved from 265.967268 at iteration 1 to 80.293942 at iteration 25, with a final archive size of 7. A 69.81% reduction in ITAE is reported.

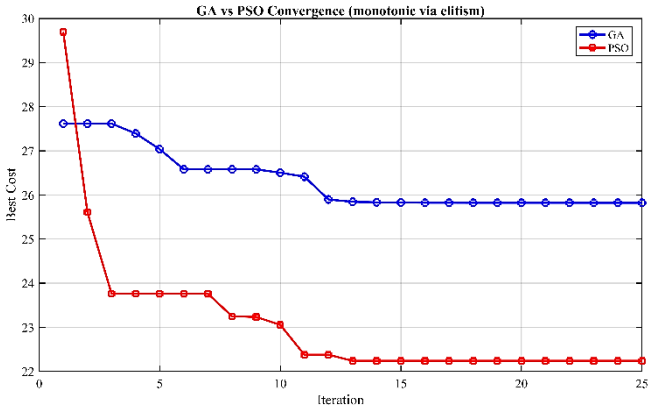

Fig. 24. Comparison of GA and PSO convergence; the cost for GA decreased from 27.615303 to 25.819880, and the cost for PSO decreased from 29.692369 to 22.237794.

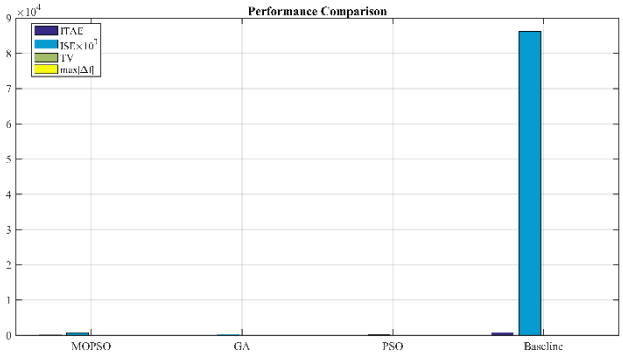

Fig. 25. Numerical comparison of MOPSO, GA, PSO, and the baseline based on performance metrics and reported constraints.

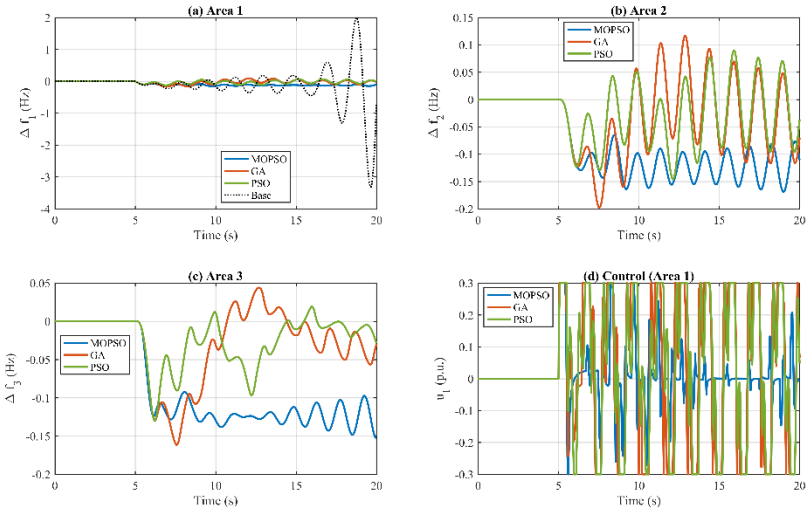

Fig. 26. Time-domain responses of the controllers.

According to *Fig. 26*, the peak values of Δf_1 for MOPSO, GA, PSO, and the baseline are 0.1605, 0.1778, 0.1251, and 3.3195, respectively. The final values of Δf_1 are -0.10659, -0.02544, -0.00983, and -0.68886, respectively.

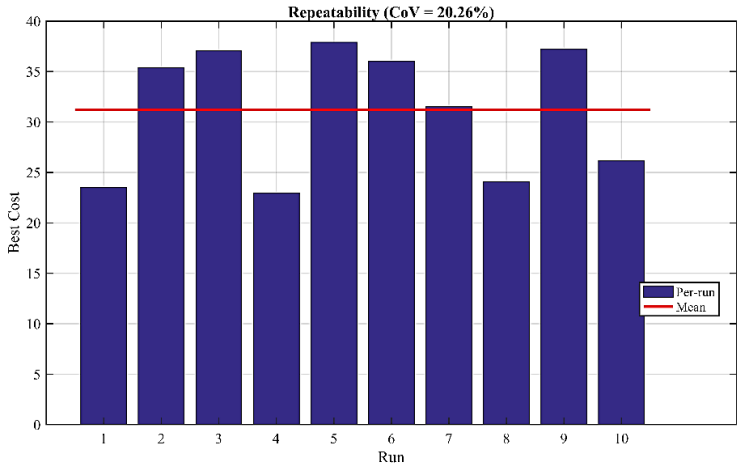

Fig. 27. Repeatability of 10 independent PSO runs.

According to *Fig. 27*, the mean is 31.1937, the standard deviation is 6.3186, and the coefficient of variation is reported as 20.26%.

5 | Closed-Loop Evaluation, Delay, and Stability

The final evaluation consists of 20 primary runs (5 controllers × 4 scenarios), 25 delay-sweep runs, 200 Monte Carlo simulations, analysis of the linearized model's poles, and a constraint verification. The five controllers compared are Proportional–Integral–Derivative (PID), T1-FPID, IT2-FPID, FOGT2-b1, and FOGT2-Adp. The closed-loop scenarios differ from the baseline model: Scenario S1 involves a load step applied at t=5s; S2 introduces a wind disturbance in Area 1; S3 features a Process Variable (PV) step at t=10s; and S4 incorporates a combination of these disturbances. The delay sweep utilizes values of τ = 0, 50, 100, 150, and 200 ms. The Monte Carlo analysis for the PID and FOGT2-Adp controllers comprised 100 paired runs, incorporating ±50% variations in H and D.

5.1 | Performance Comparison and Constraint Violations

The execution-data archives indicate that fractional-order memory affects the closed-loop response, as the ITAE values obtained with the FOGT2-Adp controller differ from those of FOGT2-b1 in all four scenarios. Specifically, the differences, defined as ITAE(FOGT2-Adp) − ITAE(FOGT2-b1), are [0.71483701, 2.4122148, 2.8655018, 3.429844]. These positive values indicate that FOGT2-Adp yields a higher ITAE than FOGT2-b1 in every scenario under the current calibration. Furthermore, the differences ITAE(PID) − ITAE(FOGT2-Adp) are [−5.7944549, 8.2061213, −3.9289591, 9.5366412]. Thus, the PID controller achieves a lower ITAE than FOGT2-Adp in Scenarios S1 and S3, whereas FOGT2-Adp achieves a lower ITAE in Scenarios S2 and S4. These results do not support the claim that the proposed controller provides the best performance across all scenarios. Instead, they indicate that the relative performance of the controllers depends on the disturbance scenario and the evaluation metric.

In the selected calibration, the PID controller violated both defined limits, with a maximum $|\Delta f|$ of 0.2366023 Hz and a maximum $|\Delta P_{tie}|$ of 0.10247591. FOGT2-Adp also exceeded the 0.20 Hz limit in scenario S3, reaching a maximum $|\Delta_f|$ of 0.20126397 Hz. These values should not be truncated or omitted; the violation of constraints constitutes a valid part of the scientific findings. Furthermore, the results for FOGT2-b1 and IT2-FPID in the primary tables are identical, which is consistent with setting β=1 and applying an α-plane of 0 in the reported implementation. This structural equivalence should not be interpreted as two distinct, independent results.

5.2 | Delay-Time Analysis and Monte Carlo Simulation

In the data archive for $\tau = 150$ ms and $\tau = 200$ ms, all five controllers were deemed invalid, exhibiting infinite ITAE values and NaN (Not a Number) steady-state values; consequently, the data do not support a stable delay tolerance of up to 200 ms. At $\tau = 100$ ms, frequency peaks in the range of 103 to 104 Hz were observed. The adaptive type-reduction selection strategy, on its own, failed to resolve this performance breakdown.

In the Monte Carlo simulation, 100 out of 100 runs for the PID controller and 100 out of 100 runs for the FOGT2-Adp controller were recorded as valid. The mean ITAE was 126.29831 (with a standard deviation of 1.2431464) for the PID controller, and 131.45981 (with a standard deviation of 1.2620647) for the FOGT2-Adp controller. In this specific test set, the comparison favours the PID controller in terms of mean ITAE; however, the number of valid runs alone does not necessarily imply superior performance quality.

5.3 | Linearized Stability Analysis

In the linearized closed-loop pole analysis, the PID controller was found to be unstable, with the maximum real part of its poles equal to 0.005813647. In contrast, the T1-FPID, IT2-FPID, FOGT2-b1, and FOGT2-Adp controllers satisfied the stability criterion applied to the linearized model. For the FOGT2-Adp controller, the Gain Margin (GM) was [value to be specified], while the phase margin (PM) was 64.228196°. These findings should be interpreted with caution, as the linearized analysis does not fully capture the effects of nonlinearities and dynamic characteristics, including saturation, dead areas, rate limits, fractional-order memory, and communication delays. Consequently, the results do not establish the overall stability of the nonlinear closed-loop system under time delays and actuator constraints; this requires further analysis using methods that explicitly account for these effects.

Performance metrics reported in related studies also vary considerably with respect to system configuration, modeling assumptions, disturbance conditions, controller architecture, and evaluation criteria. For example, the results reported for islanded microgrid controllers [1], hybrid power systems [2], parallel control architectures [3], adaptive fractional-order controllers [4], Type-2 fuzzy controllers for nonlinear systems [9], general Type-2 fractional-order PID controllers [5], interconnected microgrids [8], systems subject to time delays [6], and adaptive Type-2 control strategies [7] were obtained under different experimental or simulation conditions. Accordingly, the supplementary comparison table is intended to contextualize the proposed framework in relation to the architectures and methodological approaches adopted in previous studies, rather than to establish a direct quantitative ranking of controller performance. Similarly, Darvish Falehi [10] investigated a fractional-order Type-2 fuzzy control structure for LFC using multi-objective optimization. However, the numerical results of that study cannot be directly compared with those obtained in the present work unless the underlying models, objective functions, constraints, disturbance scenarios, and evaluation protocols are sufficiently aligned.

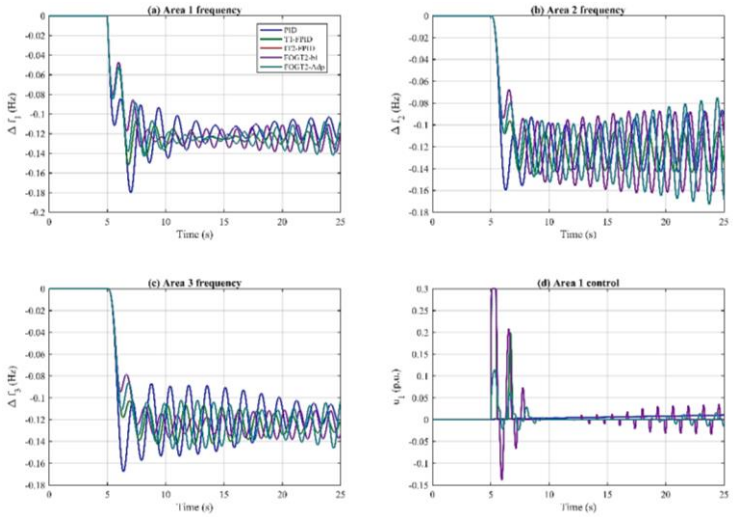

Fig. 28. Response of Scenario 1 to a step load in Area 1 during the closed-loop test; precise metrics are provided in the appended tables.

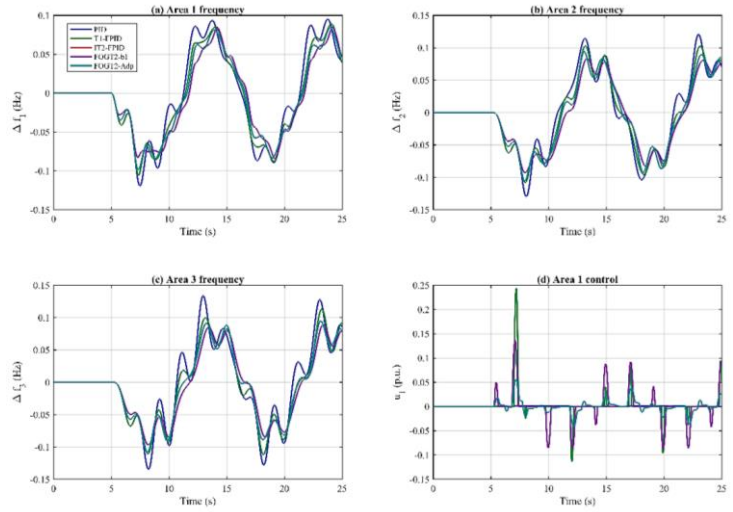

Fig. 29. Response of Scenario 2 to wind fluctuation in Area 1 during closed-loop evaluation.

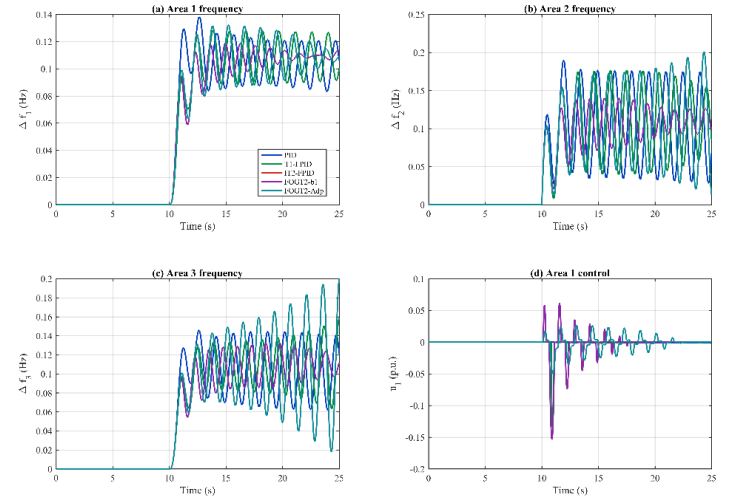

Fig. 30. Response of Scenario 3 to a PV step in Area 2; the maximum |Δf| for FOGT2-Adp is 0.20126397 Hz, which is slightly beyond the 0.2 Hz limit.

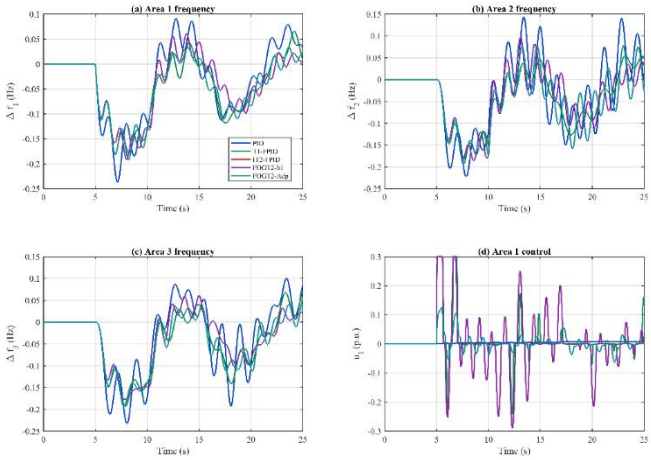

Fig. 31. Response of Scenario 4 to combined disturbances in a closed-loop evaluation.

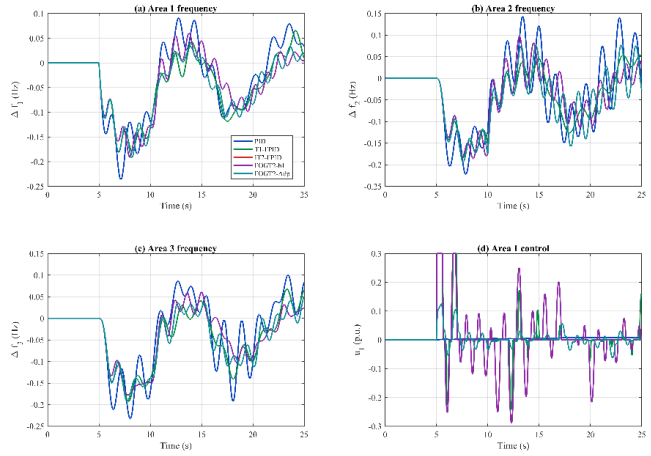

Fig. 32. Response of Scenario 4 to combined disturbances in a closed-loop evaluation.

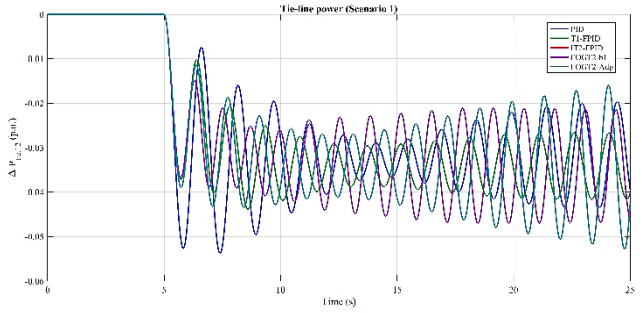

Fig. 33. Tie-line power in Scenario 1 for the evaluation of the controllers.

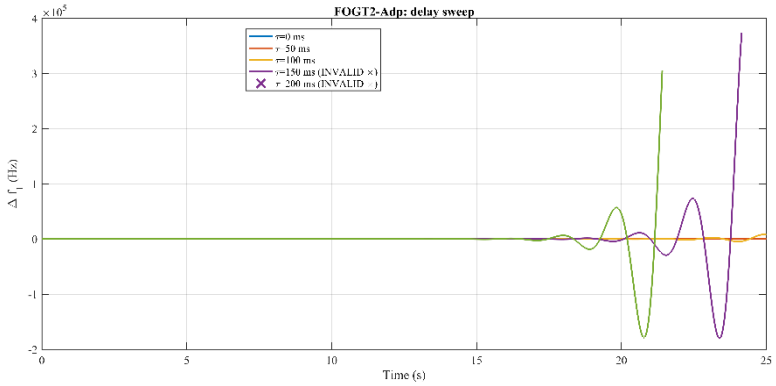

Fig. 34. Delay sweep for FOGT2-Adp; invalid runs in the original figure are marked with an 'X'.

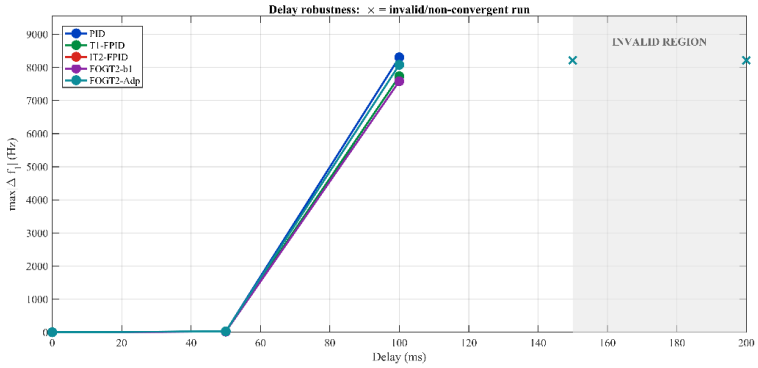

Fig. 35. Comparison of delay tolerance of the controllers; the invalid area in the original figure is shaded.

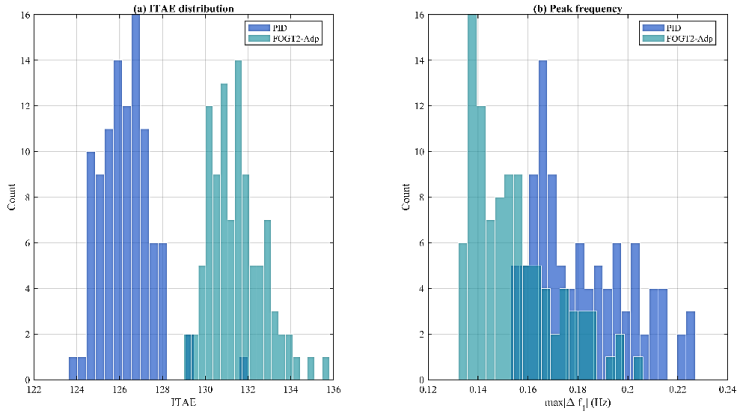

Fig. 36. Distribution of results from 200 Monte Carlo runs for the evaluated controllers.

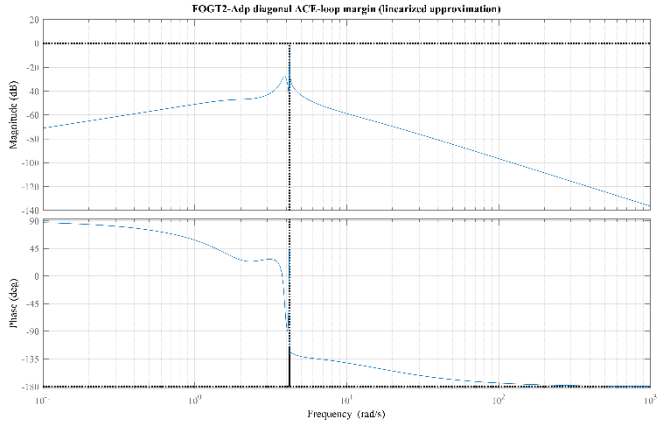

Fig. 37. Gain and phase margins of the ACE diagonal loop for FOGT2-Adp; "GM" = InfdB and "PM" = 64.228196°.

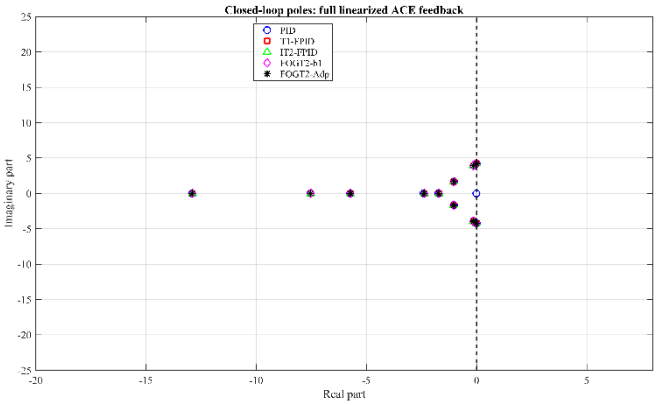

Fig. 38. Closed-loop poles in the fully linearized ACE feedback model; the PID controller has one pole with a maximum real part of 0.005813647, whereas the other four models are stable in the linearized test.

6 | Discussion and Limitations of the Study

Three categories of findings emerging from the eight evaluations should be distinguished. First, the numerical validation of the fuzzy logic components provides evidence supporting the correct implementation of the two type-reduction blocks: The NT method, evaluated using the specified α-plane representation, and the KM algorithm, whose results agree with direct calculations. Second, with respect to system modelling and simulation, the single-area model reproduces the expected steady-state error, and the two MATLAB/Simulink implementations exhibit consistency within the reported discrepancies. However, the steady-state agreement criterion specified for the three-area model is not satisfied, indicating that the model has not yet been fully validated against this criterion. Third, the closed-loop evaluations show that fractional-order memory affects the controller's output behaviour but does not consistently improve its performance under the current calibration. Specifically, the FOGT2-Adp controller fails to reduce the ITAE relative to the specified reference configuration across the four evaluated scenarios and violates the frequency-deviation constraint in scenario S3.

Comparisons among MOPSO, GA, and conventional PSO also require careful interpretation. MOPSO generates a Pareto archive from which a compromise solution is selected, whereas the GA and PSO results are obtained by optimizing a weighted cost function. Because these approaches differ fundamentally in their objective formulations, the best value of an individual performance metric obtained by one method cannot, by itself, establish its overall superiority over the others. Moreover, the observed 20.26% variability in PSO

repeatability indicates that reporting only the best run is insufficient to establish the algorithm's robustness. A more reliable comparison would require repeated independent runs and the reporting of appropriate statistical measures of performance variability.

On the basis of the available evidence, claims of uniform controller superiority or guaranteed tolerance to communication delays of up to 200 ms are not justified. A stronger assessment would require comparative optimization under identical objective functions, system models, constraints, and evaluation protocols. Further investigations should examine sensitivity to the fractional order, memory length, controller calibration parameters, and communication delay. In addition, the physical constraints should be verified across all operating scenarios, and an independent stability analysis should account explicitly for communication delays and system nonlinearities. These requirements represent limitations of the present study and directions for future work; they should not be interpreted as analyses already completed or results already established.

7 | Conclusion

This study proposed and evaluated an integrated framework for LFC in a three-area renewable-based power system. The framework combines an open-loop dynamic model, a GT2FS, NT and KM type-reduction methods, a fractional-order memory post-filter, delay-dependent method selection, and multi-objective parameter optimization. The baseline model was evaluated under four disturbance scenarios and five distinct communication-delay conditions.

The numerical validation yielded a steady-state error of (6.13663009297 \times 10^{-11}) Hz for the single-area model. For the three-area system, however, the discrepancy between the analytical equilibrium and the simulated value at t = 60s was 0.00138842712 Hz, exceeding the prescribed threshold of 10^{-3} Hz. Within the GT2FS, the fractional-order post-filter reproduced the NT output with a reported error of zero under the evaluated conditions, while the KM bounds agreed exactly with the results of direct computation. The MOPSO algorithm generated seven Pareto-optimal solutions, from which a compromise solution was selected for closed-loop evaluation.

Despite these methodological and numerical results, the closed-loop simulations revealed important performance limitations. The FOGT2-Adp controller exhibited a higher ITAE than the FOGT2-b1 controller in all four disturbance scenarios. Although the PID controller achieved lower ITAE values in scenarios S1 and S3, it violated the prescribed frequency-deviation and tie-line power constraints. The FOGT2-Adp controller also marginally exceeded the allowable frequency-deviation limit in scenario S3. Furthermore, none of the evaluated controllers maintained stability under communication delays of 150 and 200ms. Linearized analysis indicated that four controller configurations satisfied the stability criterion applied to the linearized model, whereas the PID configuration did not. These findings should be interpreted within the scope of the analysis, since linearized stability results alone do not establish the stability of the nonlinear closed-loop system under communication delays and actuator constraints.

Overall, the principal contribution of this study lies in the integration of general Type-2 fuzzy inference, multiple type-reduction approaches, fractional-order memory, and delay-dependent selection within a unified LFC framework. However, the current results do not establish the uniform performance superiority or substantial delay robustness of the proposed adaptive controller. Further work should prioritize controller recalibration, benchmarking under consistent objective functions and constraints, sensitivity analysis, and stability assessment that explicitly accounts for communication delays and system nonlinearities. These steps are necessary to determine the conditions under which the proposed framework can deliver reliable frequency regulation in renewable-based multi-area power systems.

Funding

No funds, grants, or other support were received.

Data Availability

The data are available from the corresponding author upon reasonable request.

Conflicts of Interest

The authors declare no conflicts of interest concerning the research, authorship, or publication of this article.

References

[1] Shirali, S., Zolfaghari Moghaddam, S., & Aliasghary, M. (2025). An interval Type-2 fuzzy fractional-order PD-PI controller for frequency stabilization of islanded microgrids optimized with CO algorithm. *International journal of electrical power & energy systems*, *164*, 110422. https://doi.org/10.1016/j.ijepes.2024.110422

[2] Bhatta, S. K., Mohapatra, S., Sahu, P. C., Swain, S. C., & Panda, S. (2023). Novel QO-PFA governed FO-type-II fuzzy controller for LFC of thermo-electric generator based hybrid power system. *E-prime - advances in electrical engineering, electronics and energy*, *5*, 100249. https://doi.org/10.1016/j.prime.2023.100249

[3] Aryan, P., & Raja, G. L. (2022). Design and analysis of novel QOEO optimized parallel fuzzy FOPI-PIDN controller for restructured AGC with HVDC and PEV. *Iranian journal of science and technology, transactions of electrical engineering*, *46*(2), 565–587. https://doi.org/10.1007/s40998-022-00484-7

[4] Halim, Y. M. A., Omar, O. A. M., Attia, M. A., Diaaeldin, I. M., Badr, A. O., & Afifi, M. A. (2025). Robust fractional-order adaptive cascaded strategy for mitigating load frequency deviations in renewable thermal hybrid systems. *Scientific reports*, *15*(1), 35232. https://doi.org/10.1038/s41598-025-21454-z

[5] Shi, J. Z. (2020). A fractional order general Type-2 fuzzy PID controller design algorithm. *IEEE access*, *8*, 52151–52172. https://doi.org/10.1109/ACCESS.2020.2980686

[6] Wu, H., & Zhao, T. (2022). Design of interval type-2 fuzzy fractional order pid controller based on particle swarm optimization. *Journal of physics: Conference series* (Vol. 2258, pp. 12063). IOP science. https://doi.org/10.1088/1742-6596/2258/1/012063

[7] Mohammadi, M., Peimani, M., Rasooli Saghai, H., & Shokouhandeh, H. (2026). Robust adaptive interval Type-2 fuzzy control for frequency regulation in power systems with high renewable penetration under uncertainties. *International journal of energy research*, *2026*(1), 1509413. https://doi.org/10.1155/er/1509413

[8] Ding, A., & Liu, T. (2026). Enhancing frequency stability in interconnected microgrids via a two-degree-of-freedom interval Type-2 fuzzy control strategy. *IET renewable power generation*, *20*(1), e70322. https://doi.org/10.1049/rpg2.70322

[9] Patel, H. R., & Shah, V. A. (2022). A metaheuristic approach for interval type-2 fuzzy fractional order fault-tolerant controller for a class of uncertain nonlinear system. *Automatika*, *63*(4), 656–675. https://doi.org/10.1080/00051144.2022.2061818

[10] Darvish Falehi, A. (2026). Promoted load frequency control system using optimal multi-objective design of fractional-order interval type-II fuzzy controller. *Opsearch*, *63*(2), 1261–1283. https://doi.org/10.1007/s12597-025-00937-7